ELSEVIER

Check for updates

Engineering V$_O$-Ti ensemble to boost the activity of Ru towards water dissociation for catalytic hydrogen generation

Ruofan Shen [a], Yanyan Liu [b,c,*], Hao Wen [a], Tao Liu [d], Zhikun Peng [a], Xianli Wu [a], Xianghong Ge [a], Sehrish Mehdi [a,e], Huaqiang Cao [f], Erjun Liang [a,**], Jianchun Jiang [c,**], Baojun Li [a,**]

[a] School of Physics and Microelectronics, College of Chemistry, Zhengzhou University, Zhengzhou 450001, PR China
[b] College of Science, Henan Agricultural University, Zhengzhou, Henan 450002, PR China
[c] National Engineering Lab. for Biomass Chemical Utilization, Institute of Chemical Industry of Forest Products, Chinese Academy of Forestry, Nanjing 210042, PR China
[d] CAS Key Laboratory for Biomedical Effects of Nanomaterials and Nanosafety, National Centre for Nanoscience and Technology, Beijing 100190, PR China
[e] Department of Chemistry, The Women University, Kutchery Campus, L.M.Q. Road, Multan 66000, Pakistan
[f] Department of Chemistry, Tsinghua University, Beijing 100084, PR China

ARTICLE INFO

ABSTRACT

High activity catalysts used for eliminating the energy barrier in water breaking-up are of great significance for accelerating those reactions retarded by water molecules dissociation. In this work, an oxygen vacancy (V$_O$)-Ti ensemble engineering on Ru catalyst was established to boost the catalytic activity toward water dissociation. The V$_O$ in V$_O$-Ti ensemble plays as electron promoter to transfers electrons to surface Ru atoms. The rich electron state of Ru boosts the catalytic activity toward water dissociation. As an experimental verification, the turnover frequency of 1.5-RTV$_O$-4 in ammonia borane hydrolysis reaches up to 1370 min^{-1} (9710 min^{-1} depend on the dispersion of Ru), exceeding the benchmark value set up by Ru-based catalysts. This research provides a novel electronic tuning strategy for V$_O$ as imaginary atom via electron promoter effect to enhance the intrinsic catalytic activity of metal catalysts toward inert molecule dissociation in the next generation energy chemistry field.

1. Introduction

The dissociation of water molecule plays a vital role in clean energy industry as a universally significant rate-determining step (RDS) in coal-based gas chemistry [1,2], Water–Gas Shift Reaction (WGSR), biomass reform, and renewable hydrogen energy conversion [3–7]. Up to date, the problem of high energy consumption in water molecule dissociation remains a severe challenge facing to energy utilization because of the thermal dynamically stable state of water molecule and prominent kinetics energy barrier of O—H bonds [8–14]. Therefore, exploring catalysts to break down rate-determining energy barriers is urgently for efficient conversion of resources and energy [15–22]. In the catalytic water conversion or dissociation, the rational design and construction of the catalyst is beneficial for accelerating the reaction rate and improving the overall energy efficiency. Nowadays, the activation energy of water molecule are reduced usually by constructing single-atom, inducing multicomponent synergistic effect and tailoring surface structure of

catalysts [23–25]. These groundbreaking research have effectively improved the ability of catalysts to accelerate those reactions depending water molecule dissociation. However, some flaws such as harsh reaction conditions, catalyst deactivation, complex catalytic components and difficulty in mechanism interpretation urgently need to be addressed. Novel high-efficient catalytic process for the activation and dissociation of water molecule under mild condition remains great challenging and desiring.

Oxygen vacancy (V$_O$) was observed to display somewhat potential to effectively alter the localization charge distribution and electronic energy levels near defect sites in metal oxides. These electron alternating effects express some clues indicating a possible mechanism via electron promoter effect [26]. Constructing V$_O$ can improve the ability of catalyst to activate reactive molecules in WGSR reaction [27]. The introduction of V$_O$ shows a significant effect on electron transfer and electronic interaction between active metal and support in WGSR catalysts. More effective catalytic active sites lead to efficient dissociation of water

molecules [28]. V_O-exciting catalysts exhibit capability for effective activation of water and nitrogen molecules and enhancement of energy efficiency in photocatalytic ammonia synthesis [29]. As the most important pioneer research, the electrons gathering effect in V_O is responsible for high efficient active sites in water and nitrogen molecule activation [30]. Also, V_O works for increasing the surface carriers concentration in catalysts to promote the charge transfer in oxygen and hydrogen evolution reaction [31]. Almost simultaneously, Park pointed out that the introduction of V_O endows the subject catalysts with effective regulation of electronic structure, optimized electrical conductivity, more active sites, and overall enhanced ability to dissociate water molecule [32]. In these valuable pioneering research, the V_O-containing/involving structures have been demonstrated to be promising catalyst promoter through several mechanisms displaying some important potential applications. Thus, the unique physical and chemical properties of V_O ensure an important role in the catalysis of water molecule dissociation. However, most of the above-mentioned V_O-containing catalysts require the stimulation of external fields (light, current and heat) to drive the catalytic process [33–37]. The need for energy from the external field limits the practical applications of V_O-based strategy in catalyst design. Substantial research effort should be devoted to the exploration of catalytic potential of V_O under external field-free environment on rationally designed catalytic interfacial structures. Some studies suggest that a single crystal face ensures the necessary homogeneity of V_O. The highly adjustable crystal surface and V_O concentration of TiO_2 possesses significant advantage among those known materials [38]. V_O in single crystal facet-exposed TiO_2 nanosheets is conducive to accurate insights into the role of V_O in catalysts and catalysis.

Immediately capturing reaction intermediates is necessary for evaluating the ability of catalysts to dissociate water molecules. Ammonia borane (AB) can be easily used to capture the reaction intermediates under mild conditions. The corresponding hydrolysis is beneficial to investigate the effect of V_O on the ability of catalyst to dissociate water molecules [39,40]. Ru metal or Ru-based alloy nanoparticles show excellent activity for the activation of AB. In spite of this, the ability to dissociate water molecule still needs to be improved [41–44]. Recently, most efforts on improving the activity of Ru-based catalysts are limited in those V_O-free catalytic systems. A high catalytic activity of Ru/TiO_2 (B) with the turnover frequency (*TOF*) of 303 min^{-1} demonstrates TiO_2 (B) nanotubes as suitable donor for nanoparticle immobilization [43]. The small Ru particles formed by using P25 as the supports become an outstanding active catalyst toward AB hydrolysis with the *TOF* of 558 min^{-1} in Ru and TiO_2 systems [44]. These achievements provide useful references for the correct evaluation on the future V_O-involving catalyst design approaches to efficiently promote water dissociation.

Herein, a new function of V_O to boost the catalytic activity toward water molecule dissociation via electron promoter is determined. In a TiO_2-Ru catalyst, V_O as imaginary atom is introduced onto single facet-exposed TiO_2 surface to construct V_O-Ti ensemble. Electron transfer from V_O in V_O-Ti ensemble to surface Ru adjusts the electron density of $4d$ orbital of Ru atoms. This electron-rich Ru surface caused by V_O is the origin of the boosting intrinsic activity in catalyst toward water dissociation. Besides, the V_O-Ti ensemble provides a valuable method for accelerating AB hydrolysis via promoting water dissociation. An unprecedented *TOF* of 9710 min^{-1} (1370 min^{-1} based on the overall Ru content) was achieved on 1.5-RTV$_O$-4. This *TOF* value represents the most outstanding catalytic activity compared with the reported catalyst systems composed of TiO_2 and Ru. This research verifies that engineering V_O-Ti ensemble plays an promisingly imperative role in achieving extraordinary catalytic activity of catalysts toward water dissociation and relating energy conversion fields.

2. Experimental section

2.1. Chemicals

All chemical reagents were purchased from commercial suppliers and used without further purification. The specifications are as follows, ammonia borane (NH_3BH_3, AB, United Boron, 97%), tetra-n-butyl titanate ($C_{16}H_{36}O_4Ti$, TBOT, Aladdin, 99.0%), hydrofluoric acid solution (HF, Macklin, 40 *wt.* %), ethanol solution (Sinopharm Chemical Reagent Co., Ltd., AR), sodium hydroxide (NaOH, Aladdin Industrial Co., Ltd., ACS, 97%), silicon dioxide (SiO_2, AR 99.0%, Aladdin), aluminum oxide (Al_2O_3, AR, Q/H 3396–91), tungsten trioxide (WO_3, AR, Q/12HB 4026–2006) and deionized water.

2.2. Preparation of TiO_2

The anatase TiO_2 nanosheets (denoted as TiO_2-NS) were synthesized by following procedure. HF (4 mL) and TBOT (25 mL) were mixed and stirred vigorously for 1 h. Then the mixture was added into a Teflon-lined autoclave (50 mL) and treated at 200 °C for 24 h. After being cooled to room temperature (25 °C), TiO_2-NS was centrifuged from the suspension by a high-speed centrifuge (10000 rpm, 5 min) and rinsed with alcohol several times. Then anatase TiO_2-NS was dried in a vacuum drying oven for 24 h at 60 °C.

2.3. Preparation of catalyst

The x wt. % Ru ($x = 0.5$, 1, 1.25, 1.5, 1.75 and 2.0) were supported on TiO_2-NS by simple liquid phase reduction (denoted as x-RT). TiO_2-NS (200 mg) and $RuCl_3 \cdot 3H_2O$ (15.68 mg mL^{-1}, 503 μL) were ultrasonically dispersed in deionized water for 30 min. The mass fraction of Ru in different catalysts analyzed by inductively coupled plasma-optical emission spectroscopy (ICP-OES) were summarized. Then Ru^{3+} was reduced by sodium borohydride ($NaBH_4$, 0.03 g) under further stirring for 2 h. After centrifugation, washing and drying, 1.5-RT (199.4 mg) was obtained. Similar procedures were adopted for preparation of other 0.5-RT (198.8 mg), 1.0-RT (199.0 mg), 1.25-RT (199.2 mg), 1.75-RT (199.6 mg) and 2.0-RT (200.1 mg) samples, except the different amounts of $RuCl_3 \cdot 3H_2O$ (166, 333, 418, 558 and 674 μL) solution and $NaBH_4$ (0.01 g, 0.02 g, 0.025 g, 0.035 g and 0.04 g), respectively. The control samples (denoted as x-RTN) without V_O were treated at 250 °C with a ramp of 5 °C min^{-1} in a nitrogen atmosphere and then kept for further 2 h, respectively. Similarly, $Ru-Al_2O_3$, $Ru-Al_2O_3$ and $Ru-WO_3$ with Ru loading quality of 1.5 *wt.* % are prepared for comparison. And two samples (1.5-RT and 0.5-RT) were heated to 250 °C with a ramp of 5 °C min^{-1} in a hydrogen-nitrogen atmosphere (10.0 vol% hydrogen) and then kept x h ($x = 0.5$, 1.0, 1.5 and 2.0). This hydrogen-nitrogen treating process is proceeded to introduce V_O onto TiO_2-NS surface. The generated powder was referred to as 0.5-RTV$_O$ (198.5 mg) and 1.5-RTV$_O$ (199.3 mg). All flow rate of hydrogen-nitrogen mixed gas was 30 mL min^{-1}. Samples with different V_O concentrations were denoted as x-RTV$_O$-4, x-RTV$_O$-3, x-RTV$_O$-2 and x-RTV$_O$-1. 1.5-RTV$_O$-4 was treated in air under the same conditions to obtain V_O-free sample (1.5-RTA). All samples were vacuum sealed.

2.4. Characterization

All crystalline phases of as-prepared samples were characterized by X-ray powder diffraction (XRD, Bruker/D8-Advance, Cu K_α radiation, λ = 1.5418 Å) in the 2θ range from 5 to 80°. The morphology and structure of as-prepared samples were explored by high-resolution transmission electron microscope (HRTEM, FEI Themis Z G^2 F20 S-TWIN electron microscope) and operated at 200 kV. All Transmission electron microscopy (TEM) samples were prepared by depositing a drop of diluted suspension in ethanol on a copper grid coated with a carbon film. Sub-angstrom resolution high-angle annular dark-field imaging

scanning transmission electron microscopy (HAADF-STEM) images were obtained on a FEI TITAN Chemi STEM equipped with a CEOS (Heidelburg, Germany) probe corrector, operating at 200 kV. Raman spectra were recorded with A LabRAM HR Evolution Raman spectrometer (France HORIB A Jobin Yvon S.A.A.). The Brunauere-Emmette-Teller (BET) surface area of x-RT and x-RTV$_O$ were calculated according to the N$_2$ adsorption curves in P/P_0 range of 0.05–0.35. A laser excitation wavelength of 523 nm was used. The particle size distribution of the catalysts was characterized by atomic force microscopy (AFM, NanoManVS). The electron paramagnetic resonance (EPR) spectra were obtained using a Bruker A300 EPR spectrometer at X-band (≈9 GHz) at room temperature. UV–vis diffuse reflectance spectra were obtained using Persee UV–vis spectroscopy (TU-1950, BaSO$_4$ as a reference). X-ray absorption spectroscopy (XAFS) measurements for the Ru K-edge were performed in fluorescence mode on beamline 20-BM-B with electron energy of 7 GeV and an average current of 100 mA, which located in the Advanced Photon Source at Argonne National Laboratory. The radiation was monochromatized by a Si (311) double-crystal monochromator. Ti K-edge were performed by National Synchrotron Radiation Research Center. Normalized X-ray absorption near edge structure (XANES) spectra and extended X-ray absorption fine structure (EXAFS) data reduction and analysis were processed by Athena software. X-ray photoelectron spectrum (XPS) were recorded on a PHI quantera SXM spectrometer with an Al K$_\alpha$ = 1486.6 eV excitation source, where binding energies were calibrated by referencing the C 1s peak (284.8 eV) to reduce the sample charge effect. CO chemisorption was used to determine the dispersion of Ru in catalysts. This analysis was used the Quantachrome Autosorb-IQ gas adsorption analyzer. The elemental compositions were analyzed by ICP-OES (Aglient 5110) to determine the contents.

2.5. Hydrogen generation in the batch reactor

Hydrogen generation was studied with the typical water displacement method. The catalyst (10 mg) and AB (44 mg) were placed into a 25 mL round-bottom flask fixed on a magnetic stirrer. An aqueous solution of NaOH (1 mol L^{-1}, 5 mL) was rapidly injected under magnetic stirring at 25 °C. The stirring rate was fixed at 500 rpm. An inverted and water-filled gas burette in a water-filled vessel was used to monitor the volume of the evolved H$_2$. The hydrogen generation specific rates are calculated using the information in the initiating and stabilizing stages (80 mL of hydrogen generated) according to the following formula (Eq. 1):

$$TOF = \frac{n_{H2}}{\Delta t \times n_{Ru}} \qquad (1)$$

Here, n_{H2} is the mole of hydrogen evolution during the 0–80 mL, Δt is the reaction time in unit of minutes during the 0–80 mL, n_{Ru} is the mole of Ru in 10 mg catalyst. The unit of TOF is min^{-1}. The hydrogen production of AB was carried out at a magnetic stirring mode. The recycling test was conducted at 298 K. When the previous cycle of hydrogen generation was completed, and then continues to add the same amount of AB to the flask. The total number of cycles is ten times.

The recycling test followed the same protocol with the above reaction: Once the reaction was completed, the catalyst was recovered and washed three times with water and ethanol, then dried at 298 K under vacuum. The above catalytic hydrogen generation process was repeated 10 times.

2.6. Density functional theory calculations

DFT provides theoretical support for the electrons transfer from V$_O$ to ruthenium in the catalyst, thus enhancing the catalyst's ability to dissociate water molecule. The DFT calculations of the reaction mechanism are performed with the projector augmented wave method. The exchange-functional is treated using the generalized gradient approximation of Perdew-Burke-Ernzerhof functional. The cut-off energy of the plane-wave basis is set at 400 eV for optimize calculations of atoms and surface optimization. The vacuum spacing in a direction perpendicular to the plane of the catalyst is at least 10 Å. The Brillouin zone integration is performed using $3 \times 3 \times 1$ Monkhorst and Pack k-point sampling for TiO$_2$ (001) surface. The self-consistent calculations apply a convergence energy threshold of 10^{-5} eV. The maximum Hellmann-Feynman force for each ionic optimization step is 0.03 eV/Å. The equilibrium lattice constants are optimized with maximum stress on each atom within 0.03 eV/Å. Spin polarizations was considered in all calculations. In addition, it is known the vibrational frequencies of reactants and products need to be obtained. Therefore, the energies (E) of structures, including the reactants and products, can be express by: $E = E_0 + E_{ZPE}$, where E_0 is the energy of structure what's more, the enthalpy for our reaction is the energy between product and reactant. In our calculation, the transition states of reactions had been searched using TS. And the energy for reaction can be considered as the relative energy between transition state and reactant, which can be expression as: $E_a = E_{TS}\text{-}E_{reactant}$.

3. Results and discussion

3.1. Structure feature

The plot of TOF to the loading amount of Ru displays a volcano-shape correlation in the diffusion limitation-free region. (Fig. S1 and Table S1). The catalyst with 1.5 $wt.$ % Ru provided the highest TOF value [45]. This dependence proposes that the intrinsic activity of these catalysts is not exclusively related to the presence of Ru. Other components, such as the interaction between supports and metal, the distance of active sites, and the diffusion rate of reactants to the surface of catalyst, all have somewhat effects on the catalytic activity. The highly similar XRD patterns and Raman spectra show no significant difference in x-RTN (Fig. S2a and b). TEM and AFM images show that 1.5-RTN exhibits a ~40 × 40 × 4.4 nm^3 nanosheets (Fig. S3). Ru nanoparticles (NPs) is uniformly distributed on the TiO$_2$ (001) plates (Fig. S3a and b). These structures and morphology confirm the success preparation of TiO$_2$-NS supported Ru catalysts. These catalysts can be adopted as an ideal object to study the effect of V$_O$ in catalysis.

The adjusting surface properties of catalysts after V$_O$ is constructed in 0.5-RTV$_O$ and 1.5-RTV$_O$ were investigated (Fig. 1a). A symmetrical and sharp EPR signal of TiO$_2$-V$_O$ at g = 2.003 is observed after excluding the interference of Ru (Fig. 1b) [46]. In addition, single immersion in NaBH$_4$ solution at room temperature did not produce V$_O$ in TiO$_2$. And no significant signal of Ti^{3+} in TiO$_2$-V$_O$ (Fig. S4) [47]. This result confirms the achieve introduction of V$_O$ into catalysts without the phase transition or valence change in TiO$_2$. No significant difference in the size of Ru NPs (~1.9 nm) can be observed from the TEM images of 1.5-RTV$_O$-4, 1.5-RTN, 0.5-RTV$_O$-4 and 0.5-RTN (Fig. S5a–d). TEM and HAADF-STEM images of 1.5-RTV$_O$-4 and 1.5-RTN express the same hexagonal close packing phase structure (101), size and shape of Ru NPs (Fig. 1c–j). These structure features excluded the possible correlation between the size of Ru NPs and the catalytic activity. The nonperiodic valleys in electronic intensity present some missing position corresponding to oxygen atom on TiO$_2$ (001) surface (Fig. 1i). These detections about missing oxygen atoms provide a direct evidence for the existence of V$_O$ in 1.5-RTV$_O$-4. A uniformly distributed Ru atoms is observed for 1.5-RTV$_O$-4 and 1.5-RTN in element mapping images (Fig. 1k–n and Fig. S6). Besides, the surface area of 1.5-RTV$_O$-4 (75.8 m^2 g^{-1}) and 1.5-RTN (79.9 m^2 g^{-1}) is similar (Fig. S7). Based on the above analyses, V$_O$ is proposed to be exclusively responsible for the different structure and property of 1.5-RTV$_O$-4 and 1.5-RTN.

XRD patterns and Raman spectra of 1.5-RTV$_O$ and 0.5-RTV$_O$ confirm the remaining anatase phase in TiO$_2$ after introducing V$_O$ (Fig. 2a and b). The higher absorption of TiO$_2$ (340 nm) and Ru (475 nm) in 1.5-RTV$_O$-4 than 1.5-RTN are attributed to an increasing state density of Ru induced
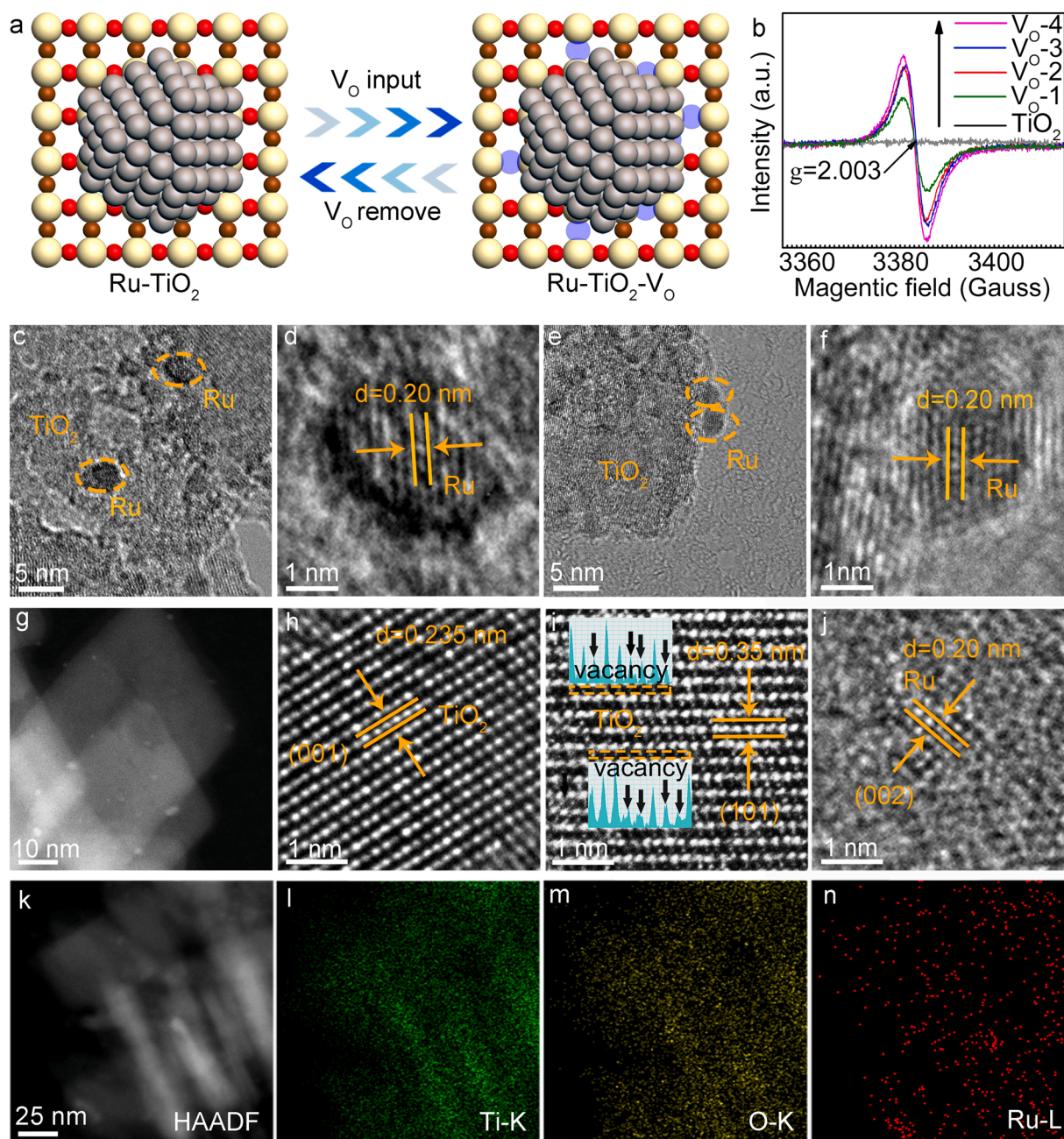
Fig. 1. Illustration of V_O introduced into catalysts (a). EPR single of TiO_2 with different V_O concentrations (b). TEM images of 1.5-RTV$_O$-4 (c, d) and 1.5-RTN (e, f). STEM images (g-j) and element mapping images (k-n) of 1.5-RTV$_O$-4.

by V_O in TiO_2 (Fig. S8). The narrowing band gap in 1.5-RTV$_O$-4 (2.8 eV) and 1.5-RTN (2.9 eV) is due to the existence of defect energy appear near the bottom of the conduction band in TiO_2 caused by V_O (Fig. 2c) [38]. The above spectroscopic analyses also prove the successful construction of V_O in 1.5-RTV$_O$-4. To get insights into the electron interaction between surface Ru atoms and V_O, XAFS investigations are carried out on 1.5-RTV$_O$-4. Compared to 1.5-RTN, the absorption edge of Ru in 1.5-RTV$_O$-4 shifts to lower photon energy (Fig. 2d). An electron-rich Ru surface induced by V_O is responsible for the lower photon energy in 1.5-RTV$_O$-4 [48]. 1.5-RTV$_O$-4, 1.5-RTN and Ru foil show the similar structure feature in k space (Fig. 2e). Fourier-transform EXAFS spectra of Ru K-edge display two major signals associated with Ru-Ru and Ru-O coordination shells (Fig. 2f). The similar Ru coordination environment in 1.5-RTV$_O$-4 and 1.5-RTN to that in Ru foil show a metallic state for Ru. The lower photon energy absorption edge of Ti in

1.5-RTV$_O$-4 than anatase TiO_2 and 1.5-RTN can be explained by the low-coordinated Ti species caused by V_O (Fig. 2g) [49]. 1.5-RTV$_O$-4 and 1.5-RTN show a similar structure feature to each other in k space (Fig. 2h). The analogous Ti coordination environments in 1.5-RTV$_O$-4, 1.5-RTN and anatase TiO_2 exclude the presence of tetrahedral coordinated Ti (Fig. 2i). Based the above analyses, the electron output from V_O in V_O-Ti ensemble to Ru is exclusively responsible for the electronic property difference of Ru surface between 1.5-RTV$_O$-4 and 1.5-RTN.

To further confirm the single electron transfer from V_O to Ru, the chemical states of catalyst surface are characterized by XPS. The peak at 531.4 eV corresponding to superoxide roots (O_2^-) is removed from TiO_2 surface after hydrogen treatment (Fig. 3a and d). A new peak emerged at 531.1 eV in 1.5-RTV$_O$-4 (Fig. 3d) [49]. This peak is attributed to Ti-OH species caused by V_O [38]. In 1.5-RTN and 1.5-RTV$_O$-4, the peaks at 458.5 eV and 464.4 eV belong to Ti^{4+}, so there is no Ti^{3+} (Fig. 3b and e).
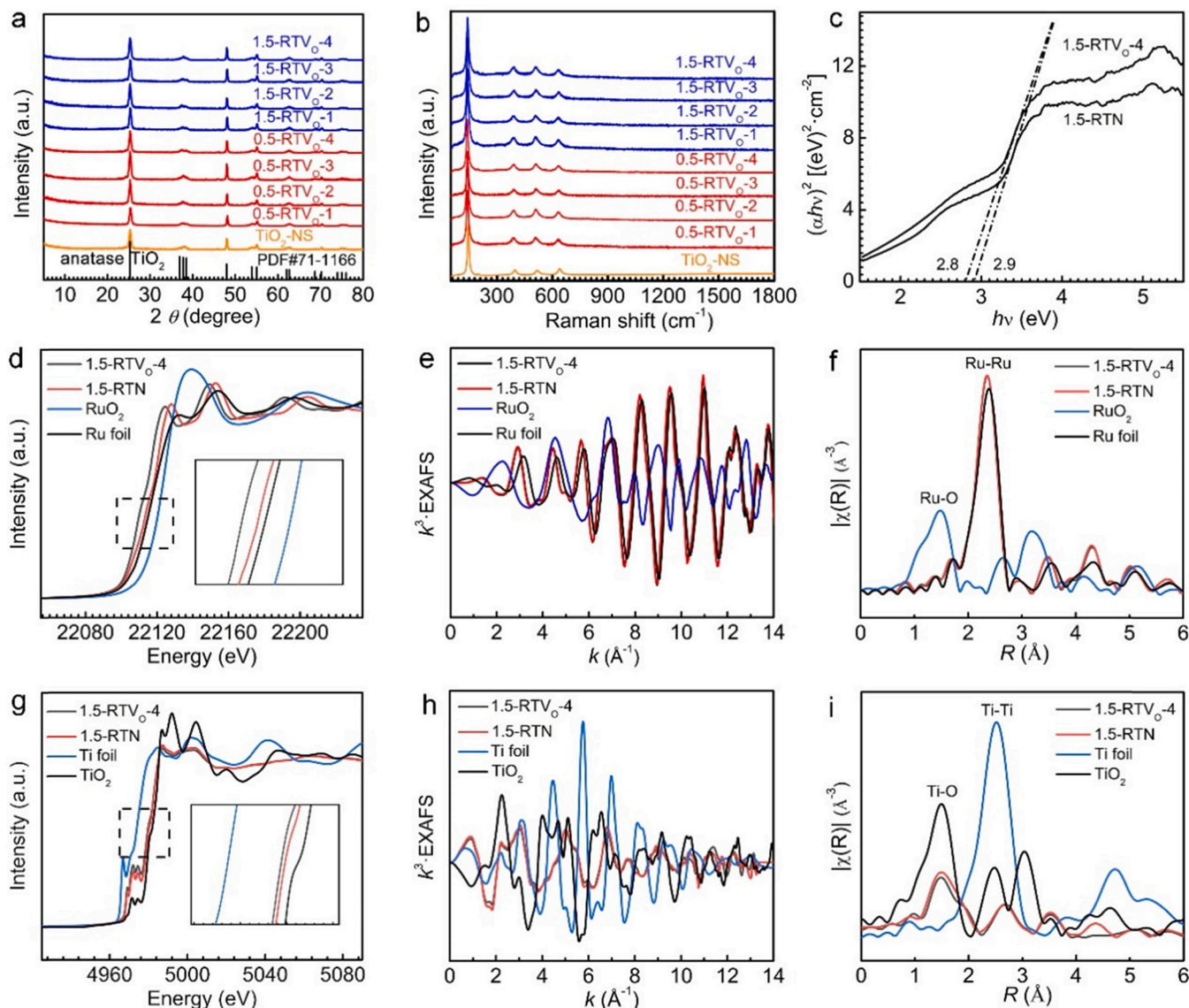
Fig. 2. The XRD patterns (a) and Raman spectra (b) of 1.5-RTV$_O$ and 0.5-RTV$_O$. The plot of $(\alpha h\nu)^2$ versus $h\nu$ curve to estimate the band gap energy of 1.5-RTV$_O$-4 (2.8 eV) and 1.5-RTN (2.9 eV) (c). XANES spectra at Ru *K*-edge for 1.5-RTV$_O$-4, 1.5-RTN, Ru foil and RuO$_2$, respectively (d). Inset: the enlarged view of absorption edge selected from (d). Fourier-transform of the extended X-ray absorption fine structure (EXAFS) spectra at Ru *K*-edge for 1.5-RTV$_O$-4, 1.5-RTN, Ru foil and RuO$_2$ in *k* and *R* spaces, respectively (e, f). Normalized XANES spectra at Ti *K*-edge for 1.5-RTV$_O$-4, 1.5-RTN, Ti foil and TiO$_2$, respectively (g). Inset: the enlarged view of absorption edge selected from (g). Fourier-transform of EXAFS spectra at Ti *K*-edge for 1.5-RTV$_O$-4, 1.5-RTN, Ti foil and TiO$_2$ in *k* and *R* spaces, respectively (h, i).

Because the amount of V$_O$ introduced is relatively small, Ti atoms still maintain a complete coordination structure (Fig. 2g), and the weak changes in Ti electronic properties caused by V$_O$ cannot be observed by XRD and XPS (Fig. 2a, b and Fig. 3e). The binding energy of Ru 3d$_{3/2}$ and Ru 3d$_{5/2}$ at 284.3 eV and 281.0 eV suggest a zero valence to Ru in 1.5-RTN (Fig. 3c). Compared with 1.5-RTN, the Ru in 1.5-RTV$_O$-4 exhibited a lower binding energy (284.2 eV and 280.6 eV) (Fig. 3f). The electron energy of the V$_O$ on TiO$_2$ is higher than that of the lattice oxygen. And the decreased work function of TiO$_2$ induced by the introduction of V$_O$, electrons easily tend to transfer from V$_O$ to the surface Ru atoms. The electron-rich Ru is responsible for the decreased Ru binding energy [50,51]. In addition, such changes in valence states of Ti and V$_O$ caused by electron transfer from V$_O$ to Ru have not been detected by XPS due to the low loading amount of Ru. The above spectral analyze are agreed with EPR and EXAFS results. Electrons transfer from V$_O$ to Ru atoms considerably adjusts the unoccupied Ru 4d orbital, exciting electron-rich surface state. This electron-rich Ru surface caused by V$_O$ in V$_O$-Ti ensembles is inferred to boost the catalytic activity toward water

dissociation in AB hydrolysis [52].

3.2. Catalytic performances

From the comparison of EPR spectra, V$_O$ concentrations are positively correlated with *TOF* values in 1.5-RTV$_O$ and 0.5-RTV$_O$ (Fig. 4a and b). The highest V$_O$ concentration resulted in the most significantly boosted *TOF* of catalysts (Fig. 4c and d). The *TOF* of catalysts with 1.5 *wt.* % Ru loading amount burgeon from 650 min^{-1} to 1370 min^{-1}, equivalent to more than twice as much improvement. And the *TOF* of catalysts with 0.5 *wt.* % Ru increases from 346 min^{-1} to 1232 min^{-1}, equivalent to closely threefold as much improvement. The relationship between V$_O$ content change (ΔV$_O$) and *TOF* change (ΔTOF) is given (Fig. 4e and f) to describe the influence of V$_O$ change on *TOF* more accurately, and linearly fit the quantity relation between ΔV$_O$ and ΔTOF. The slope of the ΔTOF relative to ΔV$_O$ in 1.5-RTV$_O$ and 0.5-RTV$_O$ is 0.7 and 1.5, respectively (Fig. 4g). This difference shows that the positive effect of V$_O$ on the catalytic activity becomes more obvious on those
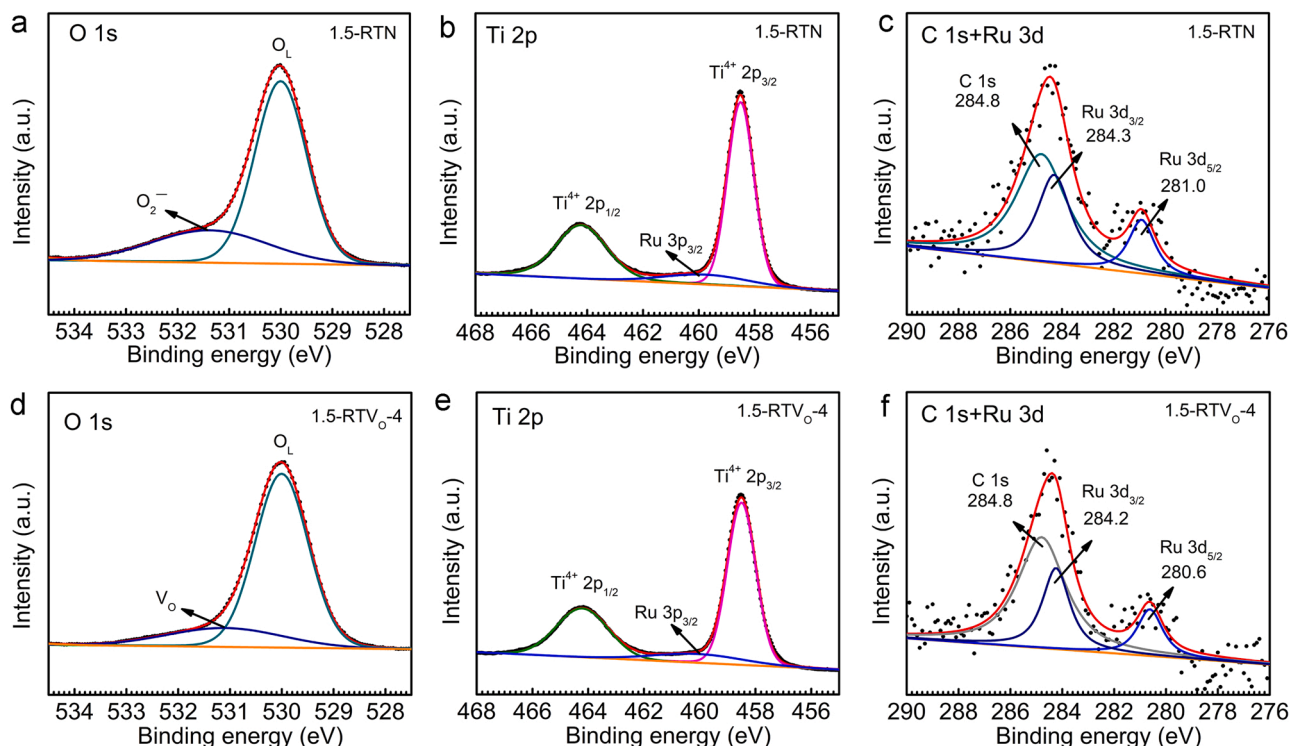
Fig. 3. XPS spectra of O 1s (a), Ti 2p (b) and Ru 3d (c) in 1.5-RTN. XPS spectra of O 1s (d), Ti 2p (e) and Ru 3d (f) in 1.5-RTV$_O$-4.

catalysts with lower loading amounts of Ru. No hydrogen is produced in the absence of Ru loading with only TiO$_2$-V$_O$, TiO$_2$ and AB solution, illustrating Ru as the key factor for the catalytic AB hydrolysis (Fig. S9a). Because of no generation of Ti^{3+} at low temperature reduction, there is no formation of coating TiO$_2$ layer through unstable Ti^{4+} species migration to Ru surface. This fact excludes the influence of classical SMSI on catalysis [53]. This work represents the highest intrinsic catalytic activity (*TOF* of 1370 min^{-1}) in the reported catalyst for other monometallic Ru catalyst systems. The *TOF* values calculated for 1.5-RTN and 1.5-RTV$_O$-4 based on Ru dispersion reach up to unprecedented 4640 min^{-1} (14.11 atm%) and 9710 min^{-1} (14.01 atm%), respectively (Table S2). Under the specified reaction conditions, AB hydrolysis rules a zero order reaction kinetics. And the introduction of V$_O$ greatly increases the reaction rate constant (*β*) (Fig. 4h). The above data confirm that the electron-rich Ru surface caused by V$_O$ greatly improves the intrinsic catalytic activity of Ru and accelerates the water dissociation in AB hydrolysis. It is difficult to produce hydrogen continuously for a long time in the laboratory, so the activity after several cycles is used to judge the stability of the catalysts. The optimized catalyst (1.5-RTV$_O$-4) is selected to test the cycle stability at 298 K. The resulted excellent *TOF* values still higher than 91.6% even after 10 cycles represent an outstanding cyclic stability (Fig. S9b). And the excellent stability of V$_O$ by adding TiO$_2$-V$_O$-4 in 10 completed cycles is confirmed by EPR result (Fig. S9c), which is responsible for the high stability of the catalyst. Besides, the surface chemical state (Fig. S10a and b) and phase structure (Fig. S10c) of the 1.5-RTV$_O$-4 remain unchanged and Ru is not lost after 10 cycles (Fig. S10d and Table S1). After removing V$_O$ in air, the activity of the sample (1.5-RTA) was still higher than that of Ru supported onto other supports (Fig. S11), showing the advantage of TiO$_2$ as the support for Ru.

To explore the overall effect of V$_O$ on the activation energy in AB hydrolysis, hydrogen generation at a series of changes in temperature are performed on specified catalysts (Fig. S12). The apparent activation energies (*E$_a$*) for 1.5-RTN, 1.5-RTV$_O$-4, 0.5-RTN and 0.5-RTV$_O$-4 are obtained to be 46.3 ($\pm$ 0.9) kJ mol^{-1}, 37.2 ($\pm$ 2.6) kJ mol^{-1}, 53.6 ($\pm$ 2.4) kJ mol^{-1} and 44.2 ($\pm$ 2.0) kJ mol^{-1}, respectively (Fig. 4i) [54].

The introduction of V$_O$ can significantly promote the activation efficiency of reactant molecules on catalyst surface in AB hydrolysis.

3.3. Catalytic mechanism

The detailed dissociation processes of H$_2$O on catalyst surface were investigated by density functional theory (DFT) simulation (Fig. 5a–d). The energy barrier for water transformation from the adsorbed state (H$_2$O*) to transition state (TS) on TiO$_2$-V$_O$-Ru surface, TiO$_2$-Ru surface, Ru surface and TiO$_2$-V$_O$ surface display a tendency as 0.21 eV<0.65 eV<0.72 eV<1.02 eV (Fig. 5e). These difference unambiguously supports that V$_O$ effectively boosts the catalytic activity toward water dissociation. The partial density of state (PDOS) of Ru 4*d* orbital in TiO$_2$-V$_O$-Ru goes up (Fig. 5f). This different PDOS demonstrated that the electron transfer from V$_O$ in V$_O$-Ti ensemble to surface Ru atoms derives a broad-range electron-rich character in the 4*d*-band occupation near Fermi level (*E$_F$*) of Ru. So the 4*d* orbital of Ru tend to overlap the anti-bond orbital of O—H in H$_2$O. The filling of anti-bond orbital weakens the O—H bond to be more easily broken. The changed PDOS can be used to explain the reduced energy barrier for H$_2$O dissociation on Ru surface. The above DFT simulation results confirm the positive role of V$_O$ in the improvement of catalytic activity to water dissociation via the formation of electron-rich Ru surface. Due to the unsaturated electrons in the orbitals of the surrounding atoms, V$_O$ has the ability of electron aggregation and special adsorption capacity. These are typical properties that oxygen atoms and other real atoms do not have. Similarly, each atomic vacancy can act as an imaginary atom, exhibiting unique properties similar to real atoms.

In the case of the catalysts used this work, DFT calculation supports the dissociation of H$_2$O molecules maybe the RDS steps in AB hydrolysis (Fig. 5e). Due to the thermodynamic difficience of direct dissociation of H$_2$O, a pre-activation induced by the acid-base interaction between partially dissociated AB molecule and adsorbed H$_2$O also is necessary for the complete dissociation of H$_2$O. The synchronous dissociation and interaction contribute the overall mechanism of AB hydrolysis [55–60]. Based on the efficient kinetics activation of H$_2$O on electron-rich Ru,
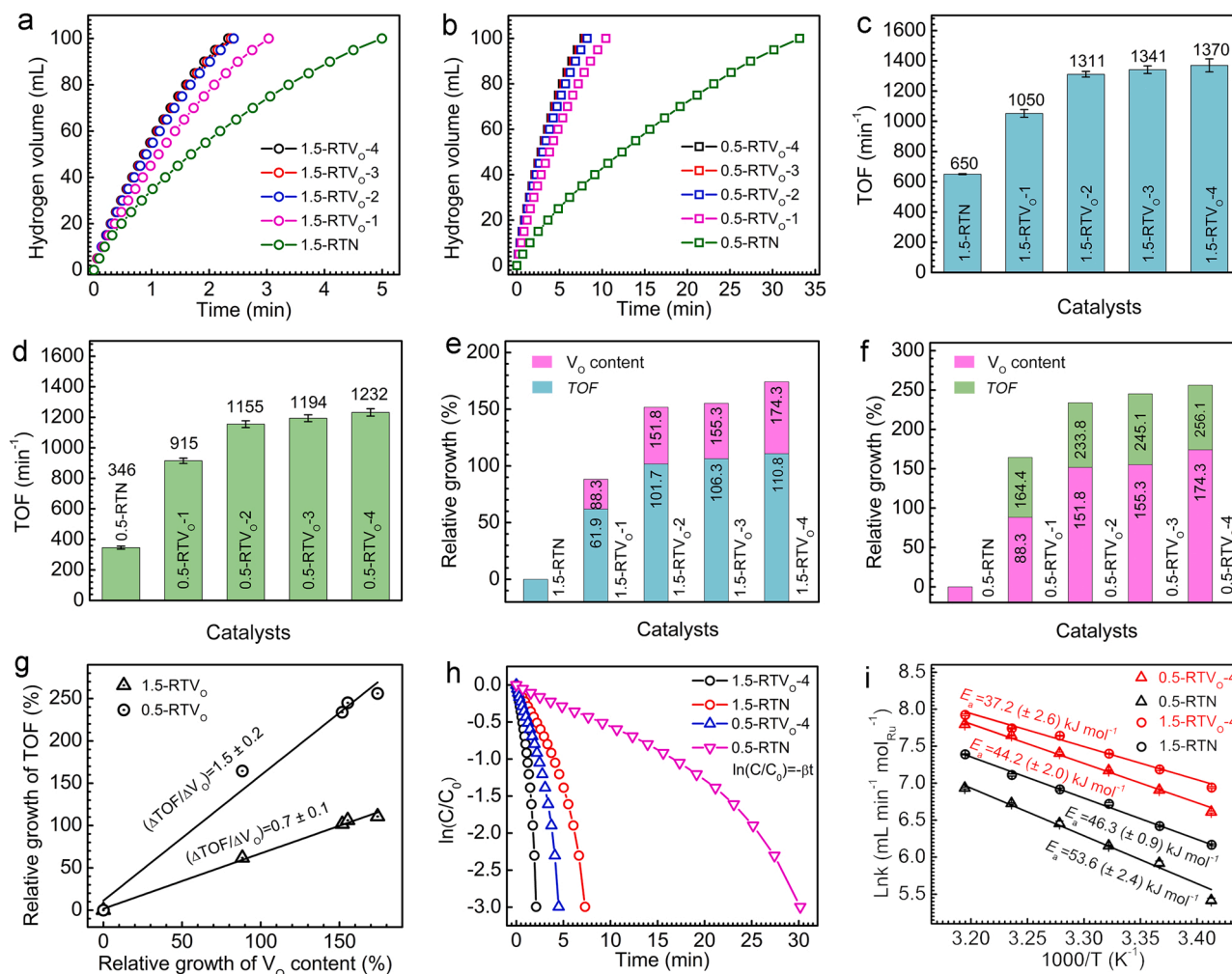
Fig. 4. Hydrogen generation at 298 K from AB by 1.5-RTV$_O$ (a) and 0.5-RTV$_O$ (b) with different V$_O$ concentrations. The *TOF* of 1.5-RTV$_O$ (c) and 0.5-RTV$_O$ (d) with different V$_O$ concentrations. The relationship between V$_O$ content change and *TOF* change in (e) 1.5-RTV$_O$ and (f) 0.5-RTV$_O$. The slope of the ΔTOF relative to ΔV_O in 1.5-RTV$_O$ and 0.5-RTV$_O$ (g). The reaction rate constant of 1.5-RTV$_O$-4 and 1.5-RTN (h). Arrhenius plot for 1.5-RTV$_O$-4, 1.5-RTN, 0.5-RTV$_O$-4 and 0.5-RTN under different temperatures (i). (Catalyst: 10 mg, AB: 44 mg, NaOH: 0.2 g, deionized water: 5 mL, 500 rpm, magneton, magnetic stirring).

H$_2$O is more easily to dissociate into OH and H on Ru, and react with AB molecules depending the thermaldynamic driving force from AB. Considering the above analyses, an overall mechanism is proposed to understand AB hydrolysis on 1.5-RTV$_O$-4 (Fig. 5g). Both activation of H$_2$O and AB take place on Ru atoms in the complete catalytic reaction. A H$_2$O molecule dissociates on Ru surface to form H* and OH*. And an NH$_3$BH$_3$ molecule approaches to Ru surface. Then the B-H bond in NH$_3$BH$_3$ is broken to form Ru-NH$_3$BH$_2$* and Ru-H*. Two H* form H$_2$ molecule on Ru surface, along with the attack of OH* to NH$_3$BH$_2$* to generate NH$_3$BH$_2$OH*. The special electronic state of V$_O$-Ti ensemble matches well to Ru in TiO$_2$-V$_O$-Ru. The high activity of electron-rich Ru toward water dissociation overcomes the rate-limiting step of AB hydrolysis and accelerates the overall hydrolysis reaction. And this electron-rich Ru induced by V$_O$ is responsible for the intrinsic catalytic activity of nanocatalysts (1.5-RTV$_O$-4). This reported level of activity surpass those of two benchmark single-atom catalysts Pt$_1$/Co$_3$O$_4$ and Rh@ZSM-5-H (Fig. 5h) [61,62]. In current reports, 1.5-RTV$_O$-4 is the highest activity toward AB hydrolysis with Ru-based catalysts (Table S3). A new function of V$_O$ as imaginary atom for boosting catalytic activity toward water molecule dissociation via electron promoter is feasible. This research provides a solid evidence for the superior potential of nanocatalysts compared with the single atom catalysts through adopting novel rational design strategy.

4. Conclusions

In conclusion, a boosting effect based on engineering V$_O$-Ti ensemble on the catalytic activity toward water dissociation is confirmed by combining the experiment and DFT simulation. The electron transfer from V$_O$ to surface Ru adjusts the electron density of 4d orbital of Ru atoms and generates electron-rich Ru. The boosted intrinsic catalytic activity toward water dissociation originates from the electron-rich Ru. The unprecedented *TOF* of 1.5-RTV$_O$-4 up to 1370 min^{-1} (9710 min^{-1} based on the dispersion of Ru), illustrates a superior overall activity of Ru catalysts in AB hydrolysis. The activity of supported Ru-based nanocatalyst surpasses those with single atom catalyst counterparts, e. g. Pt$_1$/Co$_3$O$_4$ and Rh@ZSM-5-H. This research provides a useful electronic tuning strategy for V$_O$ as imaginary atom to boost intrinsic activity of metal catalysts via electron promoter effect. A new perspective has been schematized for the improvement in the activation kinetics of water molecule and the rational design of novel high-performance catalysts.

CRediT authorship contribution statement

Ruofan Shen: Investigation, Visualization, Writing – original draft, Writing – review & editing, Formal analysis. **Yanyan Liu:** Investigation. **Hao Wen:** Investigation. **Tao Liu:** Investigation. **Zhikun Peng:**
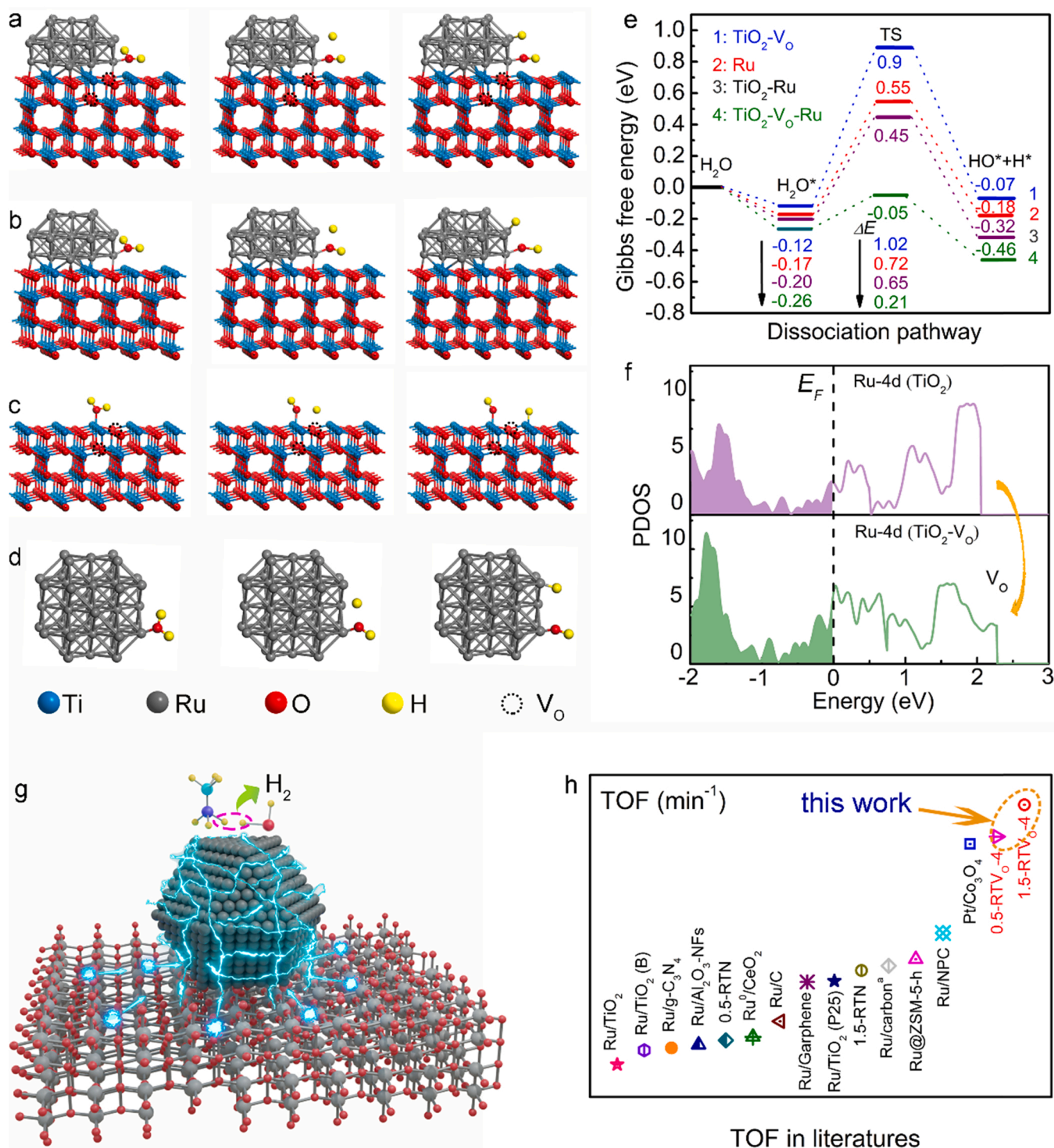
Fig. 5. The decomposition path of dissociated water on TiO$_2$-V$_O$ (a), TiO$_2$-Ru (b), TiO$_2$-V$_O$-Ru (c) and Ru (d). Potential energy surfaces and corresponding transition states for water dissociation on TiO$_2$-V$_O$-Ru, TiO$_2$-Ru, TiO$_2$-V$_O$ and Ru (e). The PDOS of Ru 4d orbital in TiO$_2$-Ru and TiO$_2$-V$_O$-Ru (f). Catalytic mechanism in the reaction system for hydrogen generation of AB on TiO$_2$-V$_O$-Ru (g). Compared with the activity of catalysts in literatures (h).

Investigation. **Xianli Wu:** Investigation. **Xianghong Ge:** Investigation. **Sehrish Mehdi:** Investigation. **Huaqiang Cao:** Investigation. **Erjun Liang:** Visualization, Formal analysis, Supervision. **Jianchun Jiang:** Visualization, Formal analysis, Supervision. **Baojun Li:** Formal analysis, Supervision, Conceptualization.

Declaration of Competing Interest

The authors declare that they have no known competing financial interests or personal relationships that could have appeared to influence the work reported in this paper.

Appendix A. Supporting information

Supplementary data associated with this article can be found in the online version at doi:10.1016/j.apcatb.2022.121100.

References

[1] J. Chen, X. Pan, H.Q. Li, H.H. Jin, J.R. Fan, Molecular dynamics investigation on supercritical water oxidation of a coal particle, Appl. Catal. B 159 (2021), 105291, https://doi.org/10.1016/j.jaap.2021.105291.

[2] H. Yan, C. Yang, W.P. Shao, L.H. Cai, W.W. Wang, Z. Jin, C.J. Jia, Construction of stabilized bulk-nano interfaces for highly promoted inverse CeO₂/Cu catalyst, Nat. Commun. 10 (2019) 3470, https://doi.org/10.1016/j.apcatb.2020.119701.

[3] M.A. Khan, I. Al-Shankiti, A. Ziani, N. Wehbe, H.A. Idriss, Stable integrated photoelectrochemical reactor for H₂ production from water attains a solar-to-hydrogen efficiency of 18% at 15 suns and 13% at 207 suns, Angew. Chem. Int. Ed. 59 (2020) 2–9, https://doi.org/10.1002/anie.202002240.

[4] C.F. Li, J.W. Zhao, L.J. Xie, J.Q. Wu, G.R. Li, Water adsorption and dissociation promoted by Co*-/N-C*-biactive sites of metallic Co/N-doped carbon hybrids for efficient hydrogen evolution, Appl. Catal. B 282 (2021), 119463, https://doi.org/10.1016/j.apcatb.2020.119463.

[5] C. Cai, S.B. Han, W. Liu, K. Sun, L. Qiao, S. Li, X.T. Zu, Tuning catalytic performance by controlling reconstruction process in operando condition, Appl. Catal. B 260 (2020), 118103, https://doi.org/10.1016/j.apcatb.2019.118103.

[6] Y. Wang, Y. Zhao, X. Ding, L. Qiao, Recent advances in the electrochemistry of layered post-transition metal chalcogenide nanomaterials for hydrogen evolution reaction, J. Energy Chem. 60 (2021) 451–479, https://doi.org/10.1016/j.jechem.2021.01.021.

[7] F. Raziq, A. Hayat, M. Humayun, S.K.B. Mane, M.B. Faheem, A. Ali, Y. Zhao, S. B. Han, C. Cai, W. Li, D.C. Qi, J.B. Yi, X.J. Yu, M.B.H. Breese, F. Hassan, F. Ali, A. Mavlonov, K. Dhanabalan, X. Xiang, X.T. Zu, S. Li, L. Qiao, Photocatalytic solar fuel production and environmental remediation through experimental and DFT based research on CdSe-QDs-coupled P-doped-g-C₃N₄ composites, Appl. Catal. B 270 (2020) 118867, https://doi.org/10.1016/j.apcatb.2020.118867.

[8] G.Q. Cui, X. Zhang, H. Wang, Z.Y. Li, W.L. Wang, Q. Yu, L.R. Zheng, Y.D. Wang, L. H. Zhu, M. Wei, ZrO₂₋ₓ modified Cu nanocatalysts with synergistic catalysis towards carbon-oxygen bond hydrogenation, Appl. Catal. B 280 (2021), 119406, https://doi.org/10.1016/j.apcatb.2020.119406.

[9] C. Wei, Y.M. Sun, G.G. Scherer, A.C. Fisher, Z.J. Xu, Surface composition dependent ligand effect in tuning the activity of nickel−copper bimetallic electrocatalysts toward hydrogen evolution in alkaline, J. Am. Chem. Soc. 142 (2020) 7765–7775, https://doi.org/10.1021/jacs.9b12005.

[10] Y.T. Wang, G.Q. Shen, Y.X. Zhang, L. Pan, X.W. Zhang, J.J. Zou, Visible-light-induced unbalanced charge on NiCoP/TiO₂ sensitized system for rapid H₂ generation from hydrolysis of ammonia borane, Appl. Catal. B 260 (2020), 118183, https://doi.org/10.1016/j.apcatb.2019.11818.

[11] T.Y. Kou, M.P. Chen, F. Wu, T.J. Smart, S.W. Wang, Y.S. Wu, Y. Zhang, S.T. Li, S. Lall, Z.H. Zhang, Y.S. Liu, J.H. Guo, G.M. Wang, Y. Ping, Y. Li, Carbon doping switching on the hydrogen adsorption activity of NiO for hydrogen evolution reaction, Nat. Commun. 11 (2020) 590, https://doi.org/10.1038/s41467-020-14462-2.

[12] C. Cai, S.B. Han, W. Liu, L. Kai. Sun, S. Qiao, X.T. Li, Zu, Tuning catalytic performance by controlling reconstruction process in operando condition, Appl. Catal. B 260 (2020), 118103, https://doi.org/10.1016/j.apcatb.2019.118103.

[13] B. Khan, F. Raziq, M. Bilal Faheem, M. Umar Farooq, S. Hussain, F. Ali, A. Ullah, A. Mavlonov, Y. Zhao, Z. Liu, H. Tian, H. Shen, X. Zu, S. Li, H. Xiao, X. Xiang, L. Qiao, Electronic and nanostructure engineering of bifunctional MoS₂ towards exceptional visible-light photocatalytic CO₂ reduction and pollutant degradation, J. Hazard. Mater. 381 (2020) 120972, https://doi.org/10.1016/j.jhazmat.2019.120972.

[14] G.Q. Cui, X. Zhang, H. Wang, Z.Y. Li, W.L. Wang, Q. Yu, L.R. Zheng, Y.D. Wang, L. H. Zhu, M. Wei, ZrO₂₋ₓ modified Cu nanocatalysts with synergistic catalysis towards carbon-oxygen bond hydrogenation, Appl. Catal. B 280 (2021), 119406, https://doi.org/10.1016/j.apcatb.2020.119406.

[15] F. Raziq, J. He, J. Gan, M. Humayun, M.B. Faheem, A. Iqbal, A. Hayat, S. Fazal, J. Yi, Y. Zhao, K. Dhanabalan, X. Wu, A. Mavlonov, T. Ali, F. Hassan, X. Xiang, X. Zu, H. Shen, S. Li, L. Qiao, Promoting visible-light photocatalytic activities for carbon nitride based 0D/2D/2D hybrid system: beyond the conventional 4-electron mechanism, Appl. Catal. B 270 (2020), 118870, https://doi.org/10.1016/j.apcatb.2020.118870.

[16] C. Chen, X. Zhu, X. Wen, Y. Zhou, S. Wang, Coupling N₂ and CO₂ in H₂O to synthesize urea under ambient conditions, Nat. Chem. 12 (2020) 1–8, https://doi.org/10.1038/s41557-020-0481-9.

[17] G. Qing, R. Ghazfar, S.T. Jackowski, F. Habizadeh, T.W. Hamann, Recent advances and challenges of electrocatalytic N₂ reduction to ammonia, Chem. Rev. 120 (2020) 5437–5516, https://doi.org/10.1021/acs.chemrev.9b00659.

[18] B.C. Filiz, A.K. Figen, S. Piskin, The remarkable role of metal promoters on the catalytic activity of Co-Cu based nanoparticles for boosting hydrogen evolution: ammonia borane hydrolysis, Appl. Catal. B 238 (2018) 365–380, https://doi.org/10.1016/j.apcatb.2018.07.03.

[19] X. Chen, X. Zhang, Y.H. Li, M.Y. Qi, J.Y. Li, Z.R. Tang, Z. Zhou, Y.J. Xu, Transition metal doping BiOBr nanosheets with oxygen vacancy and exposed {102} facets for visible light nitrogen fixation, Appl. Catal. B 218 (2021), 119516, https://doi.org/10.1016/j.apcatb.2020.119516.

[20] H.M. Liu, P. Wu, H.T. Li, Z.B. Chen, L.Z. Wang, X. Zeng, Y.X. Zhu, Y.J. Jiang, X. Z. Liao, B.S. Haynes, J. Ye, C. Stampfl, J. Huang, Unravelling the effects of layered supports on Ru nanoparticles for enhancing N₂ reduction in photocatalytic ammonia synthesis, Appl. Catal. B 259 (2019), 118026, https://doi.org/10.1016/j.apcatb.2019.118026.

[21] Y. Tang, C. Asokan, M.J. Xu, G.W. Graham, X.Q. Pan, P. Christopher, J. Li, P. Sautet, Rh single atoms on TiO₂ dynamically respond to reaction conditions by adapting their site, Nat. Commun. 10 (2019) 4488, https://doi.org/10.1021/jacs.9b12005.

[22] H. Yan, C. Yang, W.P. Shao, L.H. Cai, W.W. Wang, Z. Jin, C.J. Jia, Construction of stabilized bulk-nano interfaces for highly promoted inverse CeO₂/Cu catalyst, Nat. Commun. 10 (2019) 3470, https://doi.org/10.1038/s41467-019-11407-2.

[23] T. Ilyas, F. Raziq, S. Ali, A. Zada, N. Ilyas, R. Shaha, Y. Wang, L. Qiao, Facile synthesis of MoS₂/Cu as trifunctional catalyst for electrochemical overall water splitting and photocatalytic CO₂ conversion, Mater. Des. 204 (2021), 109674, https://doi.org/10.1016/j.matdes.2021.109674.

[24] M. Flytzani-Stephanopoulos, Gold atoms stabilized on various supports catalyze the water-gas shift reaction, Acc. Chem. Res. 47 (2014) 783–792, https://doi.org/10.1021/ar4001845.

[25] F. Raziq, M. Humayun, A. Ali, T.T. Wang, A. Khan, Q.Y. Fu, W. Luo, H.P. Zeng, Z. P. Zheng, B. Khan, H.H. Shen, X.T. Zu, S. Li, L. Qiao, Synthesis of S-Doped porous g-C₃N₄ by using ionic liquids and subsequently coupled with Au-TiO₂ for exceptional cocatalyst-free visible-light catalytic activities, Appl. Catal. B 237 (2018) 1082–1090, https://doi.org/10.1016/j.apcatb.2018.06.009.

[26] J.J. Yi, W. El-Alami, Y.H. Song, H.M. Li, P.M. Ajayan, H. Xu, Emerging surface strategies on graphitic carbon nitride for solar driven water splitting, Chem. Eng. J. 382 (2020), 122812, https://doi.org/10.1016/j.cej.2019.122812.

[27] M.S. Liang, L. Xin, L. Jiang, P. Ran, H.Z. Wang, X.Z. Chen, C.Y. Xu, S.M. Wang, J. T. Zhang, T.H. Cui, L.Q. Qu, Femtosecond laser mediated fabrication of micro/nanostructured TiO₂₋ₓ photoelectrodes: hierarchical nanotubes array with oxygen vacancies and their photocatalysis properties, Appl. Catal. B 277 (2019), 119231, https://doi.org/10.1016/j.apcatb.2020.119231.

[28] M. Xu, S. Yao, D. Rao, Y. Niu, N. Liu, M. Peng, P. Zhai, Y. Man, L. Zheng, B. Wang, B. Zhang, D. Ma, M. Wei, Insights into interfacial synergistic catalysis over Ni@TiO₂₋ₓ catalyst toward water-gas shift reaction, J. Am. Chem. Soc. 140 (2018) 11241–11251, https://doi.org/10.1021/jacs.8b03117.

[29] N. Liu, M. Xu, Y. Yang, S. Zhang, J. Zhang, W. Wang, L. Zheng, S. Hong, M. Wei, Au^{δ-}-Oᵥ-Ti^{3+} interfacial site: catalytic active center toward low-temperature water gas shift reaction, ACS Catal. 9 (2019) 2707–2717, https://doi.org/10.1021/acscatal.8b04913.

[30] J.H. Yang, Y.Z. Guo, R. Jiang, F. Qin, H. Zhang, W.Z. Lu, J.F. Wang, J.C. Yu, High-efficiency ″working-in-tandem″ nitrogen photofixation achieved by assembling plasmonic gold nanocrystals on ultrathin titania nanosheets, J. Am. Chem. Soc. 140 (2018) 8497–8508, https://doi.org/10.1021/jacs.8b03537.

[31] Z.L. Wang, X. Mao, P. Chen, M. Xiao, S.A. Monny, S.C. Wang, M. Konarova, A. Du, L.Z. Wang, Understanding the roles of oxygen vacancies in hematite-based photoelectrochemical processes, Angew. Chem. Int. Ed. 58 (2019) 1030–1034, https://doi.org/10.1002/ange.201810583.

[32] J. Sun, N. Guo, Z. Shao, K. Huang, L. Yaowen, H. Feng, Q. Wang, A facile strategy to construct amorphous spinel-based electrocatalysts with massive oxygen vacancies using ionic liquid-dopant, Adv. Energy Mater. (2018) 1800980, https://doi.org/10.1002/aenm.201800980.

[33] N. Yao, R. Meng, F. Wu, Z.Y. Fan, G.Z. Cheng, W. Luo, Oxygen-vacancy-induced CeO₂/Co₄N heterostructures toward enhanced pH-universal hydrogen evolution reactions, Appl. Catal. B 277 (2020), 119282, https://doi.org/10.1016/j.apcatb.2020.119282.

[34] M. Esmat, H. El-Hosainy, R. Tahawy, W. Jevasuwan, N. Tsunoji, N. Fukata, Y. Ide, Nitrogen doping-mediated oxygen vacancies enhancing co-catalyst-free solar photocatalytic H₂ production activity in anatase TiO₂ nanosheet assembly, Appl. Catal. B 285 (2021), 119755, https://doi.org/10.1016/j.apcatb.2020.119755.

[35] S.M. Jin, Y.H. Park, G. Bang, N.D. Vo, C.H. Lee, Revisiting magnesium oxide to boost hydrogen production via water-gas shift reaction: mechanistic study to economic evaluation, Appl. Catal. B 284 (2021), 119701, https://doi.org/10.1016/j.apcatb.2020.119282.

[36] Y. Liu, C. Ma, Q.Z. Zhang, W. Wang, P.F. Pan, L. Gu, D.D. Xu, J. Bao, Z.H. Dai, 2D electron gas and oxygen vacancy induced high oxygen evolution performances for advanced Co₃O₄/CeO₂ nanohybrids, Adv. Mater. 31 (2019) 1900062, https://doi.org/10.1002/adma.201900062.

[37] D.X. Ji, L. Fan, L. Tao, Y.J. Sun, M.G. Li, G.R. Yang, T.Q. Tran, S. Ramakrishna, S. J. Guo, The Kirkendall effect for engineering oxygen vacancy of hollow Co₃O₄ nanoparticles toward high-performance portable zinc-air batteries, Angew. Chem. Int. Ed. 131 (2019) 13978–13982, https://doi.org/10.1002/ange.201908736.

[38] F. Luo, R. Xu, S. Ma, Q. Zhang, H. Hu, K. Qu, S. Xiao, Engineering oxygen vacancies of cobalt tungstate nanoparticles enable efficient water splitting in alkaline medium, Appl. Catal. B 259 (2019), 118090, https://doi.org/10.1016/j.apcatb.2019.118090.

[39] X.B. Chen, L. Liu, P.Y. Yu, S.S. Mao, Increasing solar absorption for photocatalysis with black hydrogenated titanium dioxide nanocrystals, Science 331 (2011) 746–750, https://doi.org/10.1126/science.1200448.

[40] P. Li, R. Chen, S.E. Zhao, W.Q. Li, Y.N. Lin, Y. Yu, Architecture control and electronic structure engineering over Ni-based nitride nanocomposite for boosting ammonia borane dehydrogenation, Appl. Catal. B 295 (2021), 120523, https://doi.org/10.1016/j.apcatb.2021.120523.

[41] J.K. Zhang, W.Y. Chen, H.B. Ge, C.Q. Chen, W.J. Yan, Z. Gao, J. Gan, B.Y. Zhang, X.Z. Duan, Y. Qin, Synergistic effects in atomic-layer-deposited PtCox/CNTs catalysts enhancing hydrolytic dehydrogenation of ammonia borane, Appl. Catal. B 235 (2018) 256–263, https://doi.org/10.1016/j.apcatb.2018.04.070.

[42] Y.L. Ma, X.J. Li, Y. Zhang, L. Chen, J.T. Wu, D.J. Gao, J. Bi, G.Y. Fan, Ruthenium nanoparticles supported on TiO_2 (B) nanotubes: effective catalysts in hydrogen evolution from the hydrolysis of ammonia borane, J. Alloy. Compd. 708 (2017) 270–277, https://doi.org/10.1016/j.jallcom.2017.02.239.

[43] J. Yu, Q.J. He, G.J. Yang, W. Zhou, Z.P. Shao, M. Ni, Recent advances and prospective in ruthenium-based materials for electrochemical water splitting, ACS Catal. 9 (2019) 9973–10011, https://doi.org/10.1021/acscatal.9b02457.

[44] K. Mori, K. Miyawaki, H. Yamashita, Ru and Ru-Ni nanoparticles on TiO_2 support as extremely active catalysts for hydrogen production from ammonia-borane, ACS Catal. 6 (2016) 3128–3135, https://doi.org/10.1021/acscatal.6b00715.

[45] S. Akbayrak, S. Tanyıldızı, İ. Morkan, S.Ö. zkar, Ruthenium(0) nanoparticles supported on nanotitania as highly active and reusable catalyst in hydrogen generation from the hydrolysis of ammonia borane, Int. J. Hydrog. Energy 39 (2014) 9628–9637, https://doi.org/10.1016/j.ijhydene.2014.04.091.

[46] J. Kim, C.B. Rong, Y. Lee, J.P. Liu, S.H. Sun, From core/shell structured FePt/Fe_3O_4/MgO to ferromagnetic FePt nanoparticles, Chem. Mater. 20 (2008) 7242–7245, https://doi.org/10.1021/cm8024878.

[47] Y. Cui, K.F. Xiao, N.M. Bedford, X.X. Lu, J. Yun, R. Amal, D.W. Wang, Refilling nitrogen to oxygen vacancies in ultrafine tungsten oxide clusters for superior lithium storage, Adv. Energy Mater. 9 (2019) 1902148, https://doi.org/10.1002/aenm.201902148.

[48] H. Liu, H.T. Ma, X.Z. Li, W.Z. Li, M. Wu, X.H. Bao, The enhancement of TiO_2 photocatalytic activity by hydrogen thermal treatment, Chemosphere 50 (2003) 39–46, https://doi.org/10.1016/S0045-6535(02)00486-1.

[49] M. Xu, S. He, H. Chen, G.Q. Cui, L.R. Zheng, B. Wang, M. Wei, $TiO_{2−x}$-modified Ni nanocatalyst with tunable metal−support interaction for water−gas shift reaction, ACS Catal. 7 (2017) 7600–7609, https://doi.org/10.1021/acscatal.7b01951.

[50] J. Li, H. Zhou, H. Zhou, Z.Z. Wei, G.L. Zhuang, X. Zhong, S.D. Deng, X.N. Li, J.G. Wang, Oxygen vacancies on TiO_2 promoted the activity and stability of supported Pd nanoparticles for the oxygen reduction reaction, J. Mater. Chem. A 6 (2018) 2264–2272, https://doi.org/10.1039/C7TA09831F.

[51] H.X. Zhang, Y.F. Zhu, M. Zhao, Interface charge transfer and enhanced visible light response of graphene/anatase TiO_2 (110) systems with and without oxygen vacancy: a DFT+U calculation, Appl. Surf. Sci. 420 (2017) 105–109, https://doi.org/10.1016/j.apsusc.2017.05.142.

[52] M.M. Menamparambath, J.H. Park, H.S. Yoo, S.P. Patole, J.B. Yoo, S.W. Kim, S. Baik, Large work function difference driven electron transfer from electrides to single-walled carbon nanotubes, Nanoscale 6 (2014) 8844, https://doi.org/10.1039/c4nr01629g.

[53] H.L. Chu, N.P. Li, S.J. Qiu, Y.J. Zou, C.L. Xiang, F. Xu, L.X. Sun, Ruthenium supported on nitrogen-doped porous carbon for catalytic hydrogen generation from NH_3BH_3 hydrolysis, Int. J. Hydrog. Energy 44 (2019) 1774–1781, https://doi.org/10.1016/j.ijhydene.2018.11.101.

[54] L.X. Wang, L. Wang, X.J. Meng, F.S. Xiao, New strategies for the preparation of sinter-resistant metal-nanoparticle-based catalysts, Adv. Mater. (2019) 1901905, https://doi.org/10.1002/adma.201901905.

[55] F.Y. Fu, C.L. Wang, Q. Wang, A.M. Martinez-Villacorta, A. Escobar, H.B. Chong, X. Wang, S. Moya, L. Salmon, E. Fouquet, J. Ruiz, D. Astruc, Highly selective and sharp volcano-type synergistic Ni_2Pt@ZIF-8-catalyzed hydrogen evolution from ammonia borane hydrolysis, J. Am. Chem. Soc. 140 (2018) 10034–10042, https://doi.org/10.1021/jacs.8b06511.

[56] C.L. Wang, Q. Wang, F.Y. Fu, D. Astruc, Hydrogen generation upon nanocatalyzed hydrolysis of hydrogenrich boron derivatives: recent developments, Acc. Chem. Res. 53 (2020) 2483–2493, https://doi.org/10.1021/acs.accounts.0c00525.

[57] J.X. Feng, H. Xu, S.H. Ye, G. Ouyang, Y.X. Tong, G.R. Li, Silica-polypyrrole hybrids as high-performance metal-free electrocatalysts for the hydrogen evolution reaction in neutral media, Angew. Chem. Int. Ed. 56 (2017) 8120–8124, https://doi.org/10.1002/anie.201702934.

[58] J.X. Feng, S.-Y. Tong, Y.X. Tong, G.R. Li, Pt-like hydrogen evolution electrocatalysis on PANI/CoP hybrid nanowires by weakening the shackles of hydrogen ions on the surfaces of catalysts, J. Am. Chem. Soc. 140 (2018) 5118–5126, https://doi.org/10.1021/jacs.7b12968.

[59] S. Guan, S. An, Y. Chen, X. Liu, J. Shi, Y. Sun, Y. Fan, B. Liu, Enhancing effect of fe2 + doping of Ni/NiO nanocomposite films on catalytic hydrogen generation, ACS Appl. Mater. Interfaces 13 (2021) 42909–42916, https://doi.org/10.1021/acsami.1c12192.

[60] J.X. Feng, H. Xu, Y.T. Dong, X.F. Lu, Y.X. Tong, G.R. Li, Efficient hydrogen evolution electrocatalysis using cobalt nanotubes decorated with titanium dioxide nanodots, Angew. Chem. Int. Ed. 56 (2017) 2960–2964, https://doi.org/10.1002/anie.201611767.

[61] J.J. Li, Q.Q. Guan, H. Wu, W. Liu, Y. Lin, Z.H. Sun, X.X. Yu, X.S. Zheng, H.B. Pan, J.F. Zhu, S. Chen, W.H. Zhang, S.H. Wei, J.L. Lu, Highly active and stable metal single-atom catalysts achieved by strong electronic metal–support interactions, J. Am. Chem. Soc. 141 (2019) 14515–14519, https://doi.org/10.1021/jacs.9b06482.

[62] Q.M. Sun, N. Wang, T.J. Zhang, R. Bai, A. Mayoral, P. Zhang, Q.H. Zhang, O. Terasaki, J.H. Yu, Zeolite-encaged single-atom Rh catalysis: highly-efficient hydrogen generation and shape-selective tandem hydrogenation of nitroarenes, Angew. Chem. Int. Ed. 58 (2019) 18570–18576, https://doi.org/10.1002/anie.201912367.